

Supplemental Material: Two-Dimensional Homogeneous Fermi Gases

TRAP GEOMETRIES

The elliptic trap is formed by a highly elliptical laser beam with a wavelength of $\lambda = 1064$ nm and vertical and horizontal beam waists of approximately $w_z \approx 10$ μm and $w_y \approx 400$ μm . At a power of 1 W this results in trapping frequencies of $(\omega_x, \omega_y, \omega_z) \approx 2\pi \cdot (75, 100, 4000)$ Hz.

The hybrid box potential is formed by a superposition of several independently tunable optical and magnetic potentials, which allow for numerous different trapping geometries. In all configurations, the z -confinement with $\hbar\omega_z = h \cdot (12.4 \pm 0.1)$ kHz is realized by the lattice in z -direction, which is formed by two $\lambda = 532$ nm beams intersecting with an opening-angle of 10.4° leading to a lattice spacing of 2.9 μm . This confinement in z -direction comes with a radial anti-confinement of $\omega_{x,opt} \approx 2\pi \cdot i(9.5 \pm 1.2)$ Hz and $\omega_{y,opt} \approx 2\pi \cdot i(12.6 \pm 0.8)$ Hz.

The main contribution to the radial confinement is typically given by the repulsive ring potential, which is described in detail in the following section. An additional, harmonic confinement in radial direction is created by the curvature of the magnetic offset field used to tune interparticle interactions. A set of two coil pairs allows for tuning the curvature of the field without changing its offset. We can achieve offset fields of up to 1415 G and trap frequencies of up to $\omega_r = 2\pi \cdot 34$ Hz. This tunability thus allows us either to compensate the optical anti-confinement and create a flat-bottom trap or to provide a harmonic confinement for matter-wave imaging.

THE BOX POTENTIAL

The repulsive optical ring potential is generated by a cascaded setup of two lenses and three axicons (Fig. S1), which allows tuning the geometry of the ring independently from the beam focus. The two lenses focus the beam onto an intermediate image plane, which is then imaged onto the atoms using a high resolution objective, while the geometry of the ring is defined by the combination of the three axicons and the second lens. The first axicon splits the slightly divergent Gaussian beam into a Bessel beam in the near field and a ring beam in the far field [1]. Together with the second lens, the second axicon leads to an optical inversion of the ring beam such that the steep part of the split Gaussian beam faces towards the center of the ring (see insets in Fig. S1), resulting in a highly non-Gaussian profile. This optical inversion ensures that no residual light – which is usually present due to imperfections of the axicon tip – remains in the inner part of the ring. This has the advantage that no aperture

stop has to be placed in the beam path, which was required in previous axicon setups used for trapping ultra cold atoms [2, 3]. Finally, the third axicon collimates the geometry of the ring such that it fits within the NA of the imaging system that projects the ring onto the atoms. Moving this axicon along the optical axis allows for the size of the ring to be easily changed.

The resulting intensity distribution at the position of the atoms can be directly imaged with a second microscope objective (Fig. S2 (a)). A cut through a ring with diameter $D = 160$ μm is shown in Fig. S2 (b) and reveals the steepness of the potential wall. To obtain a measure of the steepness and gain a model for the shape of the intensity distribution, we fit a power law to one half of the cut and obtain a scaling of $V(x) = x^{87 \pm 4}$.

The flatness of the inner part of the box potential can be characterized by measuring the variation of the density $n_{2D}(\mathbf{r})$ around the mean density \bar{n}_{2D} in the ring. To do this, we take a series of images and calculate the probability of occurrence $P(n_{2D}(\mathbf{r})/\bar{n}_{2D})$ for each normalized density $n_{2D}(\mathbf{r})/\bar{n}_{2D}$ [3]. Since in a thin 2D sample the fluctuations caused by a corrugated potential can be masked by the inherent quantum fluctuations of the atomic density as well as the photonic shot noise of the imaging, averaging of a sufficient number of images is required. For our measurement we take an average of 75 density images with constant density, for which the signal to noise ratio (SNR) due to photon shot noise is approximately 29. While this makes shot noise negligible, artifacts caused by imperfections of the imaging beam still contribute to the measured fluctuations. The averaged density distribution together with the corresponding probability distribution $P(n_{2D}(\mathbf{r})/\bar{n}_{2D})$ is shown in Fig. S2. We obtain a standard deviation of the probability distribution of 8.6%.

SINGLE/DOUBLE LAYER LOADING AND DETECTION

To verify the single and double layer loading into the lattice we use a matter wave focusing technique [4]. We suddenly switch off the lattice and after a short free expansion, the elliptic trap is flashed on for 18 μs followed by a time of flight of 1 ms. The matter wave lens created by the pulse slows the z -expansion of the cloud and at the same time accelerates the different layers with respect to each other (Fig. S3 (a)). This leads to a separation of atoms in different layers after time of flight as shown in Fig. S3 (b). This provides us with a single-shot measurement of the occupation of individual layers, which is a great advantage over other techniques such as RF tomography. Tracking the occupation of individual layers over time shows that our loading scheme has low fluctuations and is stable on a timescale of several hours (Fig. S3 (c,d)).

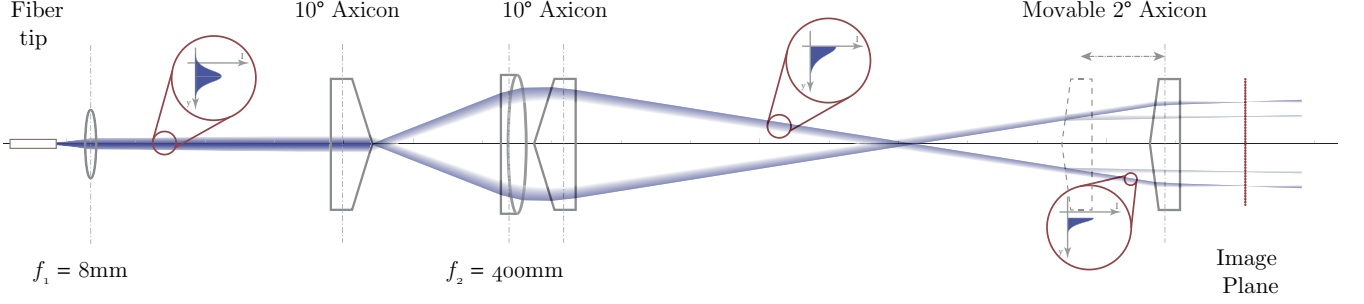


FIG. S1. Generation of the ring potential: The ring potential is generated by a setup of two lenses and three axicons with different opening angles. The two lenses image the fiber tip onto an intermediate image plane (red dotted line), which is then imaged onto the atoms using a high resolution objective (not shown). The first axicon splits the beam into a ring beam which is then optically inverted by the combination of a second axicon and the second lens. After this optical inversion the steep part of the split Gaussian beam faces towards the center of the ring. The movable third axicon collimates the geometry of the ring with a variable diameter.

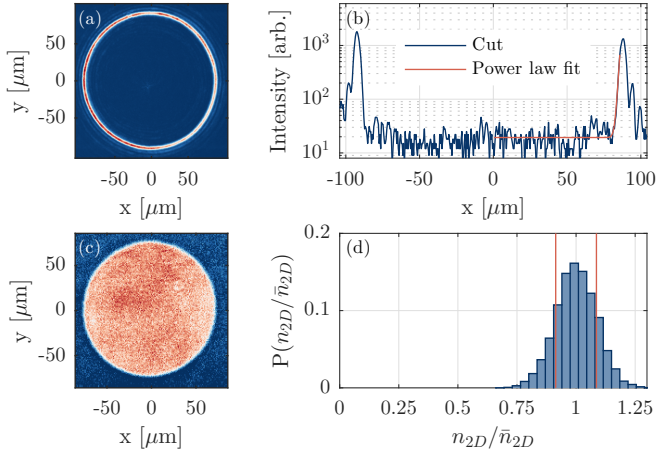


FIG. S2. Characterizing the box potential: A cut (b) through an image of the ring potential (a) reveals the steepness of the potential wall. The potential can be approximated by a power law fit $V(x) \propto x^{87 \pm 4}$. Panel (c) shows an averaged density distribution in the box potential at a magnetic offset field of 1100 G. The flatness of the box potential is quantified by calculating the probability distribution $P(n_{2D}/\bar{n}_{2D})$ for each density n_{2D} to occur (d). The result is well described by a normal distribution with a standard deviation of $\sigma = 0.086 \bar{n}_{2D}$ (red solid lines).

DENSITY DETERMINATION

The atom density $n_{2D}(\mathbf{r})$ is determined via high intensity absorption imaging [5], where we take into account three additional corrections to the modified Lambert-Beer law. We correct for the scattering of photons into the NA of the imaging system, pumping of atoms into different hyperfine states and the reduction of the absorption signal when imaging Feshbach molecules.

Absorption imaging is based on the assumption that

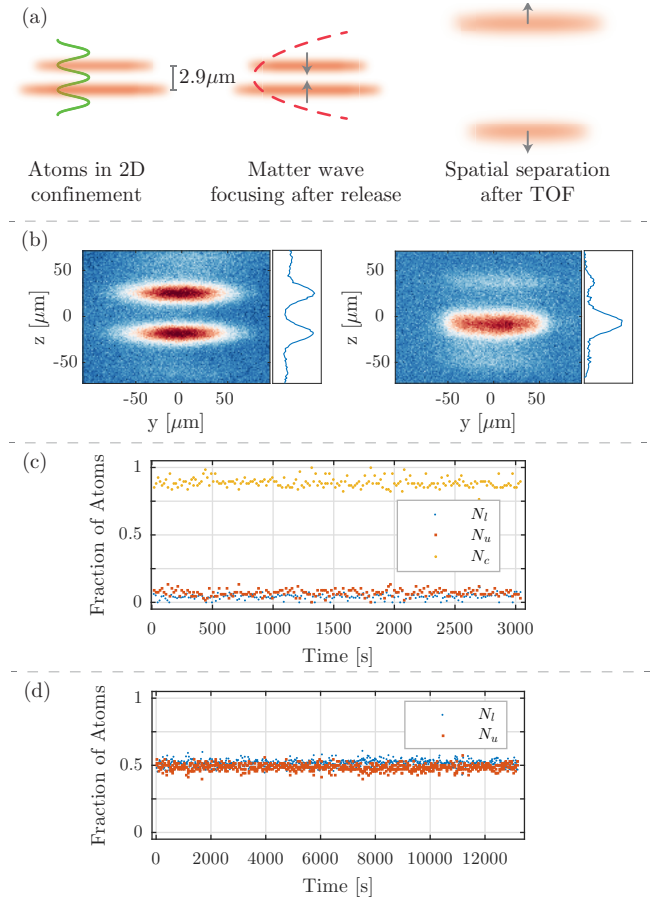


FIG. S3. Single/Double Layer Loading: Atoms in two adjacent layers are spatially separated by flashing on an attractive potential in z -direction (red dashed line) followed by a time of flight (a). The occupation of individual layers can then be determined by absorption imaging (b). Panels (c,d) show measurements of the fraction of atoms in the upper, lower and central layer (N_u, N_l and N_c) as a function of time for single and double layer loading.

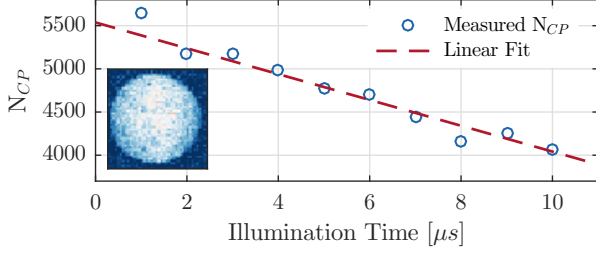


FIG. S4. Detected atom number N_{CP} in the central patch of the cloud in absorption images (inset) as a function of illumination time. The apparent atom number drops with longer illumination times as the imaging transition is not fully closed and therefore the number of atoms taking part in the scattering decreases with time (blue open circles). A linear fit (red dashed line) results in a correction factor for deducing the true atom number.

photons scattered by an atom will not be captured by the imaging system. However, in systems with a high numerical aperture, a significant fraction of the scattered photons can be recaptured by the imaging system [6]. The correction is given by $\Omega = 2\pi[1 - \cos(\theta)]/4\pi$ where $\theta = \sin^{-1}(\text{NA})$ is the opening angle defined by the NA of the imaging system. For our measurements we have chosen numerical apertures of up to $\text{NA} = 0.4$, which corresponds to a correction of 4%.

The second effect we take into account is that the $^2S_{1/2}$, $F=1/2$ to $^2P_{3/2}$, $F=3/2$ optical transition used for imaging the atoms is not fully closed. This effect is small for magnetic fields above 800 G, but becomes significant at lower magnetic fields. For our measurements of non-interacting Fermi gases at 527 G, we therefore take a reference measurement for different imaging durations (see Fig. S4) and correct the measured density accordingly.

Finally, we take into account that on the bosonic side of a Feshbach resonance, the atoms form weakly bound molecules whose binding energy increases for lower magnetic fields. As the molecules become more deeply bound, the atom-light scattering of the bound atoms is altered compared to the behavior of free atoms. We correct for this by introducing a reduced scattering cross section $\sigma_0^*(B)$ for magnetic fields ranging from 680 G to 832 G. The correction is determined by imaging samples with constant atom number at different magnetic fields.

To relate the optical density measured via absorption imaging to the atomic density $n_{2D}(\mathbf{r})$ we need to know the magnification of our imaging system. To measure the magnification we perform Kapitza-Dirac scattering on a lattice potential, which we generate by retro-reflecting the elliptic trap. This imparts a well-known momentum to the atoms, which allows us to calibrate the magnification by taking images after different times of flight. We deduce a magnification of 30.8 ± 0.3 .

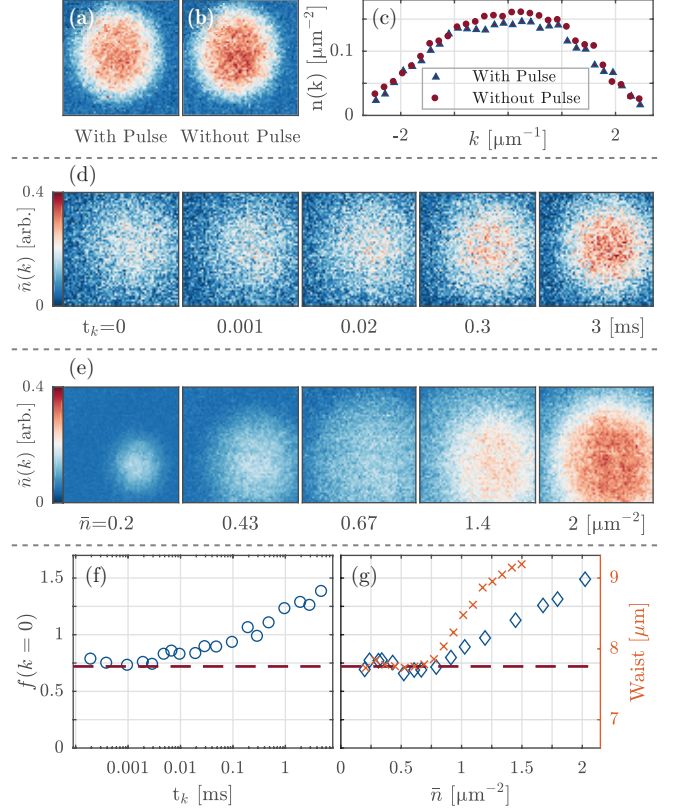


FIG. S5. Influence of collisions and transverse excited states on matter wave focusing. To prevent collisions during matter wave focusing, we remove state $|\uparrow\rangle$ using a resonant light pulse. To verify that this pulse has only negligible effects on atoms in state $|\downarrow\rangle$, we compare measurements with (a) and without (b) the pulse in a non-interacting system. Line cuts (c) through these images show that the momentum distribution of state $|\downarrow\rangle$ in a non-interacting system is not significantly altered by the optical removal pulse. For an interacting system, we map out the effect of collisions on the measured momentum distribution by waiting for a variable interaction time t_k between switching off the optical confinement and removing state $|\uparrow\rangle$. With increasing t_k , we observe a redistribution of momentum (d,f). For comparison, the central occupation obtained with $t_k = 0$ in Fig. 4 (b,c) is marked by red dashed lines. An additional source for error is that for high 2D densities, low momentum modes in higher transverse levels become occupied. We record the momentum distribution for different in situ densities \bar{n} (e) and observe an increase in central momentum occupation (blue diamonds, (g)) above a density of $\bar{n} \approx 0.75 \mu\text{m}^{-2}$. At the same density, we observe an increase in the waist of the cloud after short time of flight (red crosses), which indicates an occupation of higher transverse states.

MATTER WAVE FOCUSING OF INTERACTING 2D FERMION GASES

When measuring the momentum distribution of interacting gases using matter wave focusing, care has to be taken to ensure that the influence of interactions during the time evolution is negligible. While for a 2D gas the

density and thus the scattering rate can quickly be reduced by releasing the atoms from the strongly confining potential, the remaining collisions can nevertheless significantly affect the momentum distribution. To eliminate the influence of collisions, we remove one of the spin components, thereby effectively projecting the system onto a free Fermi gas. We accomplish this by illuminating the atoms in state $|\uparrow\rangle$ with a resonant $2\text{ }\mu\text{s}$ light pulse with an intensity of $I = I_{sat}$ before performing matter wave focusing. This removes the atoms in state $|\uparrow\rangle$ with a $1/e$ time constant of $\tau_{\uparrow} \approx 150\text{ ns}$, whereas state $|\downarrow\rangle$ has a much longer lifetime of $\tau_{\downarrow} \approx 70\text{ }\mu\text{s}$. Using a non-interacting Fermi gas, we verify that the momentum distribution of state $|\downarrow\rangle$ is not significantly altered by the light pulse (Fig. S5 (a-c)).

We then apply this method to an interacting system at $B = 1020\text{ G}$. We map out the influence of interactions on the momentum distribution by switching off the z -confinement and removing state $|\uparrow\rangle$ after different expansion times t_k . We observe that when increasing the time t_k during which collisions can take place beyond $3\text{ }\mu\text{s}$, the apparent occupation of lower momentum modes increases (see Fig. S5 (d,f)). We attribute this to collisions transferring momentum from the radial into the transverse direction.

We note that the influence of collisions on the matter wave imaged density distribution is small, as the short time during which collisions take place leaves the in situ density distribution largely unaffected. Therefore, matter wave images are not a good measure for the influence of collisions on the momentum distribution.

Finally, the dimensionality of the system has a profound impact on the momentum distribution. For low densities, our system is in the 2D regime and we find that $f(k=0)$ remains constant as we increase the density, while the width of the distribution grows. As the density surpasses a value of $\bar{n} \approx 0.75\text{ }\mu\text{m}^{-2}$, $f(k=0)$ begins to increase which we attribute to the population of higher transverse states (see Fig. S5 (e,g)). This interpretation is supported by a measurement of the transverse width of the cloud after short time of flight similar to the one described in [7]. We find that the transverse width starts to increase at the same density $\bar{n} \approx 0.75\text{ }\mu\text{m}^{-2}$, signaling the beginning of the crossover to a 3D system.

-
- [1] J. H. McLeod, J. Opt. Soc. Am. **44**, 592 (1954).
 - [2] I. Manek, Y. Ovchinnikov, and R. Grimm, Opt. Commun. **147**, 67 (1998).
 - [3] B. Mukherjee, Z. Yan, P. B. Patel, Z. Hadzibabic, T. Yefsah, J. Struck, and M. W. Zwierlein, Phys. Rev. Lett. **118**, 123401 (2017).
 - [4] P. A. Murthy, D. Kedar, T. Lompe, M. Neidig, M. G. Ries, A. N. Wenz, G. Zürn, and S. Jochim, Phys. Rev. A **90**, 043611 (2014).
 - [5] K. Hueck, N. Luick, L. Sobirey, T. Lompe, H. Moritz, L. Clark, and C. Chin, Opt. Exp. **25** (2017).
 - [6] M. Pappa, P. C. Condylis, G. O. Konstantinidis, V. Bolpasi, A. Lazoudis, O. Morizot, D. Sahagun, M. Baker, and W. von Klitzing, New J. Phys. **13**, 115012 (2011).
 - [7] P. Dyke, K. Fenech, T. Pepler, M. G. Lingham, S. Hoinka, W. Zhang, S.-G. Peng, B. Mulkerin, H. Hu, X.-J. Liu, and C. J. Vale, Phys. Rev. A **93**, 011603 (2016).